Monthly Notices
of the
ROYAL ASTRONOMICAL SOCIETY

MNRAS **486,** 3047–3058 (2019)
Advance Access publication 2019 April 3

doi:10.1093/mnras/stz955

The submillimetre view of massive clusters at $z \sim 0.8$–1.6

E. A. Cooke,[1] Ian Smail,[1,2]★ S. M. Stach,[1] A. M. Swinbank,[1,2] R. G. Bower,[1,2] Chian-Chou Chen,[3] Y. Koyama[4] and A. P. Thomson[5]

[1]*Centre for Extragalactic Astronomy, Department of Physics, Durham University, Durham DH1 3LE, UK*
[2]*Institute for Computational Cosmology, Department of Physics, University of Durham, South Road, Durham DH1 3LE, UK*
[3]*European Southern Observatory, Karl Schwarzschild Strasse 2, D-85748 Garching bei München, Germany*
[4]*Subaru Telescope, National Astronomical Observatory of Japan, National Institutes of Natural Sciences, 650 North A'ohoku Place, Hilo, HI 96720, USA*
[5]*Jodrell Bank Centre for Astrophysics, School of Physics and Astronomy, The University of Manchester, Oxford Road, Manchester M13 9PL, UK*

Accepted 2019 March 29. Received 2019 March 18; in original form 2018 December 18

ABSTRACT

We analyse 850 μm continuum observations of eight massive X-ray-detected galaxy clusters at $z \sim 0.8$–1.6 taken with SCUBA-2 on the James Clerk Maxwell Telescope. We find an average overdensity of 850-μm-selected sources of a factor of 4 ± 2 per cluster within the central 1 Mpc compared to the field. We investigate the multiwavelength properties of these sources and identify 34 infrared counterparts to 26 SCUBA-2 sources. Their colours suggest that the majority of these counterparts are probable cluster members. We use the multiwavelength far-infrared photometry to measure the total luminosities and total cluster star formation rates demonstrating that they are roughly three orders of magnitude higher than local clusters. We predict the *H*-band luminosities of the descendants of our cluster submillimetre galaxies and find that their stellar luminosity distribution is consistent with that of passive elliptical galaxies in $z \sim 0$ clusters. Together, the faded descendants of the passive cluster population already in place at $z \sim 1$ and the cluster submillimetre galaxies are able to account for the total luminosity function of early-type cluster galaxies at $z \sim 0$. This suggests that the majority of the luminous passive population in $z \sim 0$ clusters is likely to have formed at $z \gg 1$ through an extreme, dust-obscured starburst event.

Key words: galaxies: clusters: general – submillimetre: galaxies.

1 INTRODUCTION

In the local Universe, the most massive galaxies reside in the centres of galaxy clusters (e.g. Kauffmann et al. 2004; Bamford et al. 2009). These massive galaxies typically have little to no ongoing star formation, display spheroidal 'early-type' morphologies, and contain old, metal-rich stellar populations. Detailed 'archaeological' studies of the star formation histories of luminous ellipticals ($\gtrsim L^*$) indicate most of their stars were formed 8–11 Gyr ago at $z > 1$, through a series of bursts of star formation (e.g. Bower, Lucey & Ellis 1992; Thomas et al. 2005; Citro et al. 2016; González Delgado et al. 2017; see also Johnston, Aragón-Salamanca & Merrifield 2014; Cooke et al. 2015). More massive galaxies have been found to have older stellar populations (e.g. Nelan et al. 2005), and ellipticals within clusters have older stellar ages than those residing in the field (e.g. Rettura et al. 2011).

At $z \sim 1$ the cores of massive clusters appear to have already formed, and display similar properties to local clusters (e.g. Cerulo et al. 2016). Indeed, there are now several known examples of apparently passive cluster cores at $z \sim 1$–2 (e.g. Strazzullo et al. 2013; Newman et al. 2014; Cooke et al. 2016; Lee-Brown et al. 2017). However, there is also evidence that significant star formation is occurring within clusters at these epochs (e.g. Hayashi et al. 2010; Tran et al. 2010; Brodwin et al. 2013; Zeimann et al. 2013). In particular, the number of dusty star-forming galaxies in clusters, observable by their bright infrared luminosities, increases out to $z > 1$ (e.g. Best 2002; Webb et al. 2005; Geach et al. 2006; Tran et al. 2010; Popesso et al. 2012; Webb et al. 2013; Alberts et al. 2014; Noble et al. 2016). This dust-obscured star formation traces increased activity in the clusters, whose mean integrated star formation rate (SFR) appears to evolve very rapidly, $\sim(1+z)^{\gamma}$, with $\gamma \sim 6$–7 (Kodama et al. 2004; Geach et al. 2006; Koyama et al. 2010, 2011; Shimakawa et al. 2014; Ma et al. 2015), compared to the field, $\gamma = 4$ (Ilbert et al. 2015). This accelerated star formation activity means that by $z \sim 1$–1.5, clusters host significant numbers (although with large cluster-to-cluster variation) of dusty 'submillimetre galaxies' (SMGs), so-called because of their bright luminosities at submillimetre wavelengths (e.g. Tadaki et al. 2012; Ma et al. 2015).

Studies of the dusty star-forming population of cluster galaxies at $z > 1$ have been hampered by limited statistics, which often

★ E-mail: ian.smail@durham.ac.uk

Table 1. Properties of the eight clusters in our sample. The final two columns indicate the number of submillimetre sources selected in each field (Table 2), and the number of infrared-selected counterparts, including those with multiple counterparts (Table 3).

ID	RA [J2000]	Dec. [J2000]	z	σ_{850} [mJy beam^{-1}]	kT_X [eV]	$\log_{10}(M_{200})$ [$\log_{10}(M_\odot)$]	N_{850}	N_{IR}
RXJ0152−1357	01:52:44.18	−13:57:15.8	0.831	0.51	4.3 ± 0.5	14.5 ± 0.1	14	8
WARPJ1415+3611	14:15:10.48	+36:11:59.0	1.030	0.49	6.2 ± 0.8	14.7 ± 0.1	12	3
RDCSJ0910+5422	09:10:44.90	+54:22:08.9	1.100	0.59	7.0 ± 2.0	14.8 ± 0.2	14	5
RDCSJ1252−2927	12:52:54.40	−29:27:17.0	1.237	0.63	6.0 ± 0.7	14.6 ± 0.1	10	2
RXJ0849+4451	08:48:56.20	+44:52:00.0	1.261	0.89	6.0 ± 3.0	14.6 ± 0.3	5	2
XMUJ2235−2557	22:35:20.60	−25:57:42.0	1.393	0.89	6.0 ± 3.0	14.6 ± 0.3	6	2
XCSJ2215−1738	22:15:58.51	−17:38:02.5	1.450	0.64	7.0 ± 3.0	14.7 ± 0.3	10	10
XDCPJ0044−2033	00:44:05.20	−20:33:59.7	1.579	0.54	7.0 ± 1.0	14.6 ± 0.2	12	2

show starkly different results. For example, Smail et al. (2014) showed that the core of Cl J0218−0510 at $z = 1.62$ (Papovich et al. 2010; Tanaka, Finoguenov & Ueda 2010) is mostly inactive. Using the SCUBA-2 Cosmology Legacy Survey (S2CLS) map of the UKIDSS Ultra Deep Survey (UDS; Geach et al. 2017) they identified 31 probable cluster SMGs, but found that few of these lie in the core (2 Mpc diameter region), which is instead dominated by apparently passive massive red galaxies ($>L^*$ or $M_H \sim -23$; Lotz et al. 2013; Hatch et al. 2016, 2017; Lee-Brown et al. 2017). By contrast, Stach et al. (2017) and Hayashi et al. (2017) revealed 14 luminous far-infrared galaxies, with a combined star-formation rate of $>1000\,M_\odot\,yr^{-1}$, within a 500 kpc diameter region in the heart of XCS J2215.9−1738 at $z = 1.46$ (Stanford et al. 2006; Hilton et al. 2010). These observations mean that XCS J2215 is one of the most strongly star-forming clusters known to date (Stach et al. 2017; Hayashi et al. 2018). These two clusters illustrate the wide variation in the dusty star-forming population seen in distant clusters and the environments in which these systems are found.

Untangling the average evolution of massive cluster galaxies, and their likely form at high redshift, requires a larger, more uniform sample of clusters. To this end, we have undertaken a sensitive 450/850 μm survey of eight massive galaxy clusters at $0.8 < z < 1.6$ with SCUBA-2 (Holland et al. 2013) on the James Clerk Maxwell Telescope (JCMT) to search for dust-obscured highly star-forming galaxies within these massive structures and statistically measure the properties of cluster SMGs.

The layout of this paper is as follows: Section 2 outlines our observations and data reduction. In Section 3 we analyse the mid- to far-infrared properties of the observed submillimetre sources. Section 4 discusses the star formation rates and evolution of cluster SMGs with redshift. Our conclusions are presented in Section 5. Throughout we use a lambda cold dark matter (ΛCDM) cosmology with $H_0 = 70\,km\,s^{-1}\,Mpc^{-1}$, $\Omega_M = 0.3$, and $\Omega_\Lambda = 0.7$. Magnitudes are given in the AB system.

2 OBSERVATIONS AND DATA REDUCTION

Our sample is comprised of eight well-studied $z \gtrsim 1$ X-ray-detected clusters. The X-ray detections are required to ensure the selection of bound systems, and enable estimates of cluster mass and dynamical structure. The eight clusters (Table 1) were observed with SCUBA-2 simultaneously at 450 μm and 850 μm in weather conditions $\tau_{250\,GHz} < 0.08$ between 2013 April 09 and 2016 May 10. In total each cluster was observed for an average of 10 h using a standard constant-velocity daisy mapping pattern. The sensitivity in the resulting maps drops to 50 per cent at a radius of ∼5.4 arcmin from the map centre due to the scan coverage of the daisy pattern.

Individual maps for each night of observation were reduced using the Dynamic Interactive Map-Maker (DIMM) tool of the Sub-Millimetre User Reduction Facility (SMURF; Chapin et al. 2013) with the blank field configuration in order to detect point sources within the maps. The maps were calibrated using a flux conversion factor of $FCF_{450\mu m} = 491\,Jy\,beam^{-1}\,pW^{-1}$ and $FCF_{850\mu m} = 537\,Jy\,beam^{-1}\,pW^{-1}$ and then combined using inverse-variance weighting to create a final map per cluster at each wavelength. To improve point source detection, the resulting 450 μm and 850 μm maps were match-filtered with an 8 arcsec and 15 arcsec Gaussian filter, respectively. This match-filtering step in the data reduction has been shown to introduce a small (10 per cent) loss of flux from point sources (e.g. Chen et al. 2013; Geach et al. 2017). We thus apply an upward correction of 10 per cent to our measured fluxes.

At 850 μm the median noise in the centre of the maps is $0.6^{+0.3}_{-0.1}$ mJy (Table 1). The maps were cropped to radii of 2.5 arcmin, where the noise properties of the maps are low and more uniform (with a variation across the map of ∼33 per cent). This radius corresponds to approximately 1.2 Mpc at $z \sim 1.2$, the median redshift of our sample. False-colour images of the eight clusters are shown in Fig. 1. These clusters show a wide range of activity at 850 μm within the central 1 Mpc.

2.1 Source selection

To select submillimetre sources from the SCUBA-2 maps we first use AEGEAN (Hancock et al. 2012; Hancock, Trott & Hurley-Walker 2018) to identify peaks brighter than 1σ above the noise in each map and then measure fluxes from the SCUBA-2 maps. As these sources are unresolved, we then take as the flux of each source its peak flux value in each of the 450 μm and 850 μm maps. The error on this flux is the value in the corresponding pixel in the error map produced from the data reduction pipeline. Owing to the better uniformity of our 850 μm maps, we concentrate on those in the following analysis and primarily use the 450 μm data to constrain the spectral energy distributions of the 850 μm sources.

Jack-knifed maps were created using the same process detailed above but, before mosaicking, half of the individual scans were inverted in order to create maps with no astronomical signal (e.g. Weiß et al. 2009; Geach et al. 2013). We then run our detection process detailed above on these jack-knifed maps in order to estimate the contamination expected from false-positive sources in each map. Fig. 2 shows the distribution of sources as a function of their 850 μm flux for each cluster and the jack-knifed maps.

To select our sample, we apply a uniform cut of $S/N = S_{850}/\sigma_{850} \geq 4$, which selects 79 submillimetre sources and corresponds to a false detection rate in the jack-knifed maps of 11 per cent. To construct a

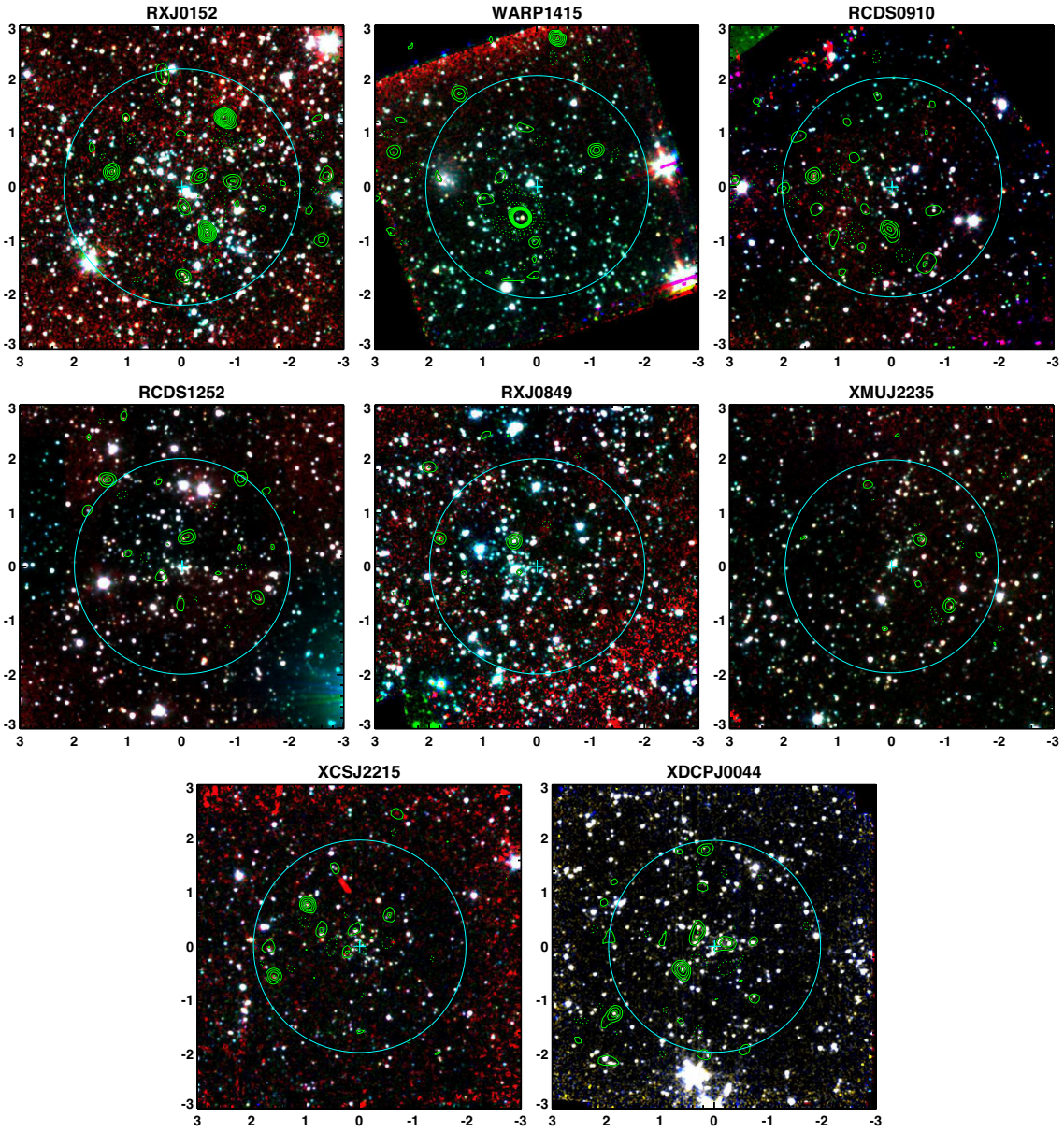

Figure 1. IRAC 3.6, 4.5, and 5.8 μm three-colour images of the eight clusters in our sample. XDCP J0044 only has coverage in two IRAC channels, so it is a false-colour 3.6 μm and 4.5 μm image. The contours show the SCUBA-2 850 μm flux; solid contours start at 3σ and increase by 2σ. The dotted contours show -3σ and -5σ. The X-ray-detected centre of each cluster is marked by a cross. The large circle denotes a 1 Mpc radius around each cluster core. We detect 83 submillimetre sources with signal-to-noise ratio (S/N) ≥ 4 or $S_{850} \geq 4$ mJy.

flux-limited sample, we also include an 'extended sample', where we select all sources with $S_{850} \geq 4$ mJy. This includes a further four sources between 4σ and 3σ, although with a false detection rate of 2, i.e. 50 per cent.

Our final submillimetre sample has 83 sources detected at either S/N $\geq 4\sigma$ or $S_{870} \geq 4$ mJy across all cluster fields, with an overall expected false detection rate of 13 per cent. The properties of the full sample are listed in Table 2.

2.2 Number counts

To calculate the expected completeness of our sample, we insert fake sources into the jack-knifed 850 μm maps for each cluster field. Fake sources are randomly placed within the maps and have fluxes distributed according to

$$\frac{\mathrm{d}N}{\mathrm{d}S} = \left(\frac{N_0}{S_0}\right)\left(\frac{S}{S_0}\right)^{\gamma} \exp\left(-\frac{S}{S_0}\right), \quad (1)$$

with $N_0 = 7180\,\mathrm{deg}^{-2}$, $S_0 = 2.5$ mJy, and $\gamma = 1.5$ (Geach et al. 2017). We then run our source detection as described above and include a source as recovered if a point source is found within the full width at half-maximum (FWHM) of the SCUBA-2 850 μm effective beam (14.6 arcsec). This is repeated 1000 times per map, giving a sample of 8000 fake sources. We then evaluate the recovery rate of fake sources as a function of 850 μm flux and use this to correct our observed number counts, shown in Fig. 3.

We also apply a flux-deboosting correction appropriate for SCUBA-2 (see Geach et al. 2017), which statistically corrects for

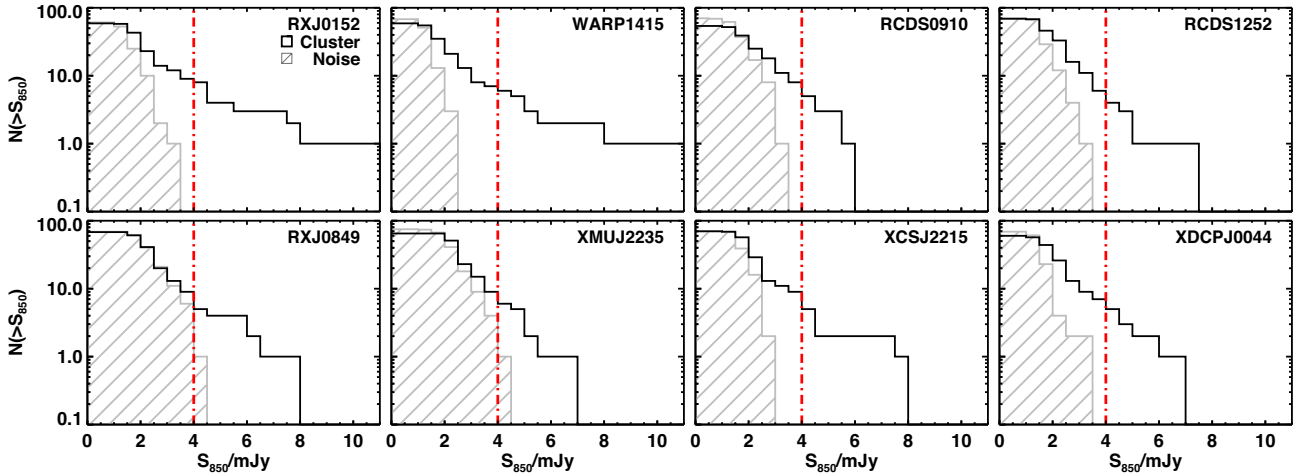

Figure 2. Cumulative number counts of submillimetre sources above a given flux density for all eight clusters. Sources detected in the SCUBA-2 maps are shown in black and sources in the jack-knifed maps are shown by the hatched grey histogram. The dot–dashed line shows the uniform 4 mJy cut we use to select sources, corresponding to $>3\sigma$ across all the maps. We also include all sources with a signal-to-noise ratio S/N $\geq$ 4, which gives an overall false-detection rate of $\sim$13 per cent.

Table 2. Table of identifications and infrared properties of SCUBA-2-identified submillimetre sources. All sources with S/N $\geq$ 4 were selected, as well as those with S/N $<$ 4 but $S_{850\mu m} > 4$ mJy. The fluxes given are observed peak fluxes for each source in the corresponding map.

ID	RA	Dec.	S_{850}	S_{450}
	[J2000]		[mJy]	[mJy]
RXJ0152_01	01:52:44.02	−13:58:53.0	4.0 ± 0.6	20 ± 5
RXJ0152_02	01:52:33.58	−13:58:13.0	3.8 ± 0.6	7 ± 5
RXJ0152_03	01:52:42.10	−13:58:05.0	7.6 ± 0.5	22 ± 4
RXJ0152_04	01:52:44.02	−13:57:37.0	3.4 ± 0.5	16 ± 4
RXJ0152_05	01:52:34.41	−13:57:41.0	2.3 ± 0.5	<4
RXJ0152_06	01:52:37.98	−13:57:41.0	2.0 ± 0.5	7 ± 4
RXJ0152_07	01:52:40.18	−13:57:09.0	4.1 ± 0.5	10 ± 4
RXJ0152_08	01:52:42.65	−13:57:01.0	4.3 ± 0.5	<4
RXJ0152_09	01:52:49.52	−13:56:57.0	7.1 ± 0.7	6 ± 5
RXJ0152_10	01:52:33.03	−13:57:05.0	4.0 ± 0.6	17 ± 5
RXJ0152_11	01:52:51.17	−13:56:33.0	3.5 ± 0.7	16 ± 5
RXJ0152_12	01:52:44.30	−13:56:17.0	2.6 ± 0.6	12 ± 5
RXJ0152_13	01:52:41.00	−13:55:57.0	10.6 ± 0.6	27 ± 5
RXJ0152_14	01:52:45.67	−13:55:09.0	5.2 ± 0.9	13 ± 6
WARP1415_01	14:15:10.77	+36:10:59.0	3.5 ± 0.5	10 ± 3
WARP1415_02	14:15:10.77	+36:10:19.0	3.4 ± 0.6	8 ± 4
WARP1415_03	14:15:10.77	+36:10:39.0	2.2 ± 0.6	7 ± 3
WARP1415_04	14:15:23.99	+36:11:07.0	4.3 ± 0.7	5 ± 4
WARP1415_05	14:15:12.09	+36:11:23.0	19.2 ± 0.5	41 ± 3
WARP1415_06	14:15:15.40	+36:11:47.0	2.9 ± 0.5	11 ± 3
WARP1415_07	14:15:13.74	+36:12:11.0	2.3 ± 0.5	4 ± 3
WARP1415_08	14:15:23.66	+36:12:39.0	4.7 ± 0.7	6 ± 4
WARP1415_09	14:15:05.15	+36:12:39.0	5.1 ± 0.5	11 ± 3
WARP1415_10	14:15:11.43	+36:13:03.0	2.2 ± 0.5	6 ± 3
WARP1415_11	14:15:17.71	+36:13:43.0	4.8 ± 0.6	15 ± 4
WARP1415_12	14:15:08.79	+36:14:47.0	7.9 ± 0.6	23 ± 4
RCDS0910_01	09:10:40.88	+54:20:44.0	3.8 ± 0.7	16 ± 4
RCDS0910_02	09:10:52.32	+54:21:16.0	3.3 ± 0.6	9 ± 4
RCDS0910_03	09:10:48.66	+54:21:04.0	2.6 ± 0.6	5 ± 4
RCDS0910_04	09:10:45.46	+54:21:24.0	6.0 ± 0.6	16 ± 4
RCDS0910_05	09:10:54.61	+54:21:44.0	3.4 ± 0.6	11 ± 4
RCDS0910_06	09:10:39.96	+54:21:44.0	3.1 ± 0.6	12 ± 4
RCDS0910_07	09:10:48.20	+54:21:44.0	2.6 ± 0.6	8 ± 4
RCDS0910_08	09:11:06.97	+54:22:07.9	5.0 ± 0.7	16 ± 5
RCDS0910_09	09:11:05.14	+54:22:15.9	4.4 ± 0.7	16 ± 5
RCDS0910_10	09:10:58.73	+54:22:07.9	4.3 ± 0.7	7 ± 4

Table 2 – *continued*

ID	RA	Dec.	S_{850}	S_{450}
	[J2000]		[mJy]	[mJy]
RCDS0910_11	09:10:55.07	+54:22:20.0	5.5 ± 0.6	21 ± 4
RCDS0910_12	09:10:49.58	+54:22:40.0	2.6 ± 0.6	9 ± 4
RCDS0910_13	09:10:56.91	+54:23:04.0	3.9 ± 0.7	15 ± 4
RCDS0910_14	09:10:50.50	+54:23:20.0	2.8 ± 0.6	15 ± 4
RCDS1252_01	12:52:54.39	−29:27:57.0	2.7 ± 0.6	17 ± 5
RCDS1252_02	12:52:47.96	−29:27:53.0	4.0 ± 0.7	12 ± 6
RCDS1252_03	12:52:56.23	−29:27:29.0	3.3 ± 0.6	23 ± 5
RCDS1252_04	12:52:58.99	−29:27:01.0	2.6 ± 0.6	19 ± 6
RCDS1252_05	12:52:54.09	−29:26:45.0	4.9 ± 0.6	13 ± 5
RCDS1252_06	12:53:02.35	−29:26:13.0	4.0 ± 0.8	16 ± 7
RCDS1252_07	12:52:47.35	−29:25:53.0	3.3 ± 0.7	<5
RCDS1252_08	12:53:00.82	−29:25:41.0	7.1 ± 0.8	16 ± 7
RCDS1252_09	12:52:49.49	−29:25:41.0	4.9 ± 0.7	15 ± 6
RCDS1252_10	12:52:59.29	−29:24:29.0	4.2 ± 0.9	<5
RXJ0849_01	08:49:13.93	+44:51:57.5	6.0 ± 1.0	10 ± 9
RXJ0849_02	08:48:58.50	+44:52:25.6	7.5 ± 0.8	15 ± 6
RXJ0849_03	08:49:06.40	+44:52:29.6	6.0 ± 0.9	23 ± 7
RXJ0849_04	08:49:07.53	+44:53:49.6	6.0 ± 1.0	<6
RXJ0849_05	08:49:01.51	+44:54:25.6	4.0 ± 1.0	13 ± 8
XMUJ2235_01	22:35:27.42	−25:57:26.0	5.0 ± 1.0	13 ± 8
XMUJ2235_02	22:35:21.49	−25:56:58.0	5.2 ± 0.9	31 ± 7
XMUJ2235_03	22:35:15.56	−25:57:02.0	6.7 ± 0.9	19 ± 7
XMUJ2235_04	22:35:30.09	−25:56:30.0	5.0 ± 1.0	13 ± 9
XMUJ2235_05	22:35:30.68	−25:55:54.0	4.0 ± 1.0	22 ± 9
XMUJ2235_06	22:35:17.64	−25:54:46.0	5.0 ± 2.0	20 ± 10
XCSJ2215_01	22:16:01.30	−17:39:35.0	4.4 ± 0.8	20 ± 6
XCSJ2215_02	22:15:59.06	−17:39:43.0	7.7 ± 0.7	26 ± 6
XCSJ2215_03	22:16:02.97	−17:38:39.0	7.4 ± 0.7	21 ± 6
XCSJ2215_04	22:16:00.74	−17:38:35.0	4.0 ± 0.7	6 ± 5
XCSJ2215_05	22:15:58.50	−17:38:19.0	3.8 ± 0.6	15 ± 5
XCSJ2215_06	22:15:59.90	−17:37:59.0	3.6 ± 0.6	17 ± 5
XCSJ2215_07	22:16:04.94	−17:37:51.0	3.6 ± 0.7	24 ± 6
XCSJ2215_08	22:15:48.43	−17:37:31.0	3.1 ± 0.8	<5
XCSJ2215_09	22:15:59.90	−17:37:19.0	4.0 ± 0.7	6 ± 5
XCSJ2215_10	22:16:06.89	−17:36:27.0	4.3 ± 0.9	16 ± 7
XDCPJ0044_01	00:44:05.97	−20:34:40.5	2.2 ± 0.5	9 ± 4
XDCPJ0044_02	00:43:57.99	−20:34:32.5	4.2 ± 0.6	6 ± 5
XDCPJ0044_03	00:44:00.56	−20:34:12.5	2.5 ± 0.5	16 ± 4
XDCPJ0044_04	00:44:10.24	−20:34:16.5	2.8 ± 0.6	12 ± 5

Table 2 – *continued*

ID	RA	Dec.	S_{850}	S_{450}
	[J2000]		[mJy]	[mJy]
XDCPJ0044_05	00:44:05.40	−20:34:12.5	3.7 ± 0.5	16 ± 4
XDCPJ0044_06	00:44:03.69	−20:33:48.5	4.2 ± 0.5	12 ± 4
XDCPJ0044_07	00:44:13.66	−20:33:44.5	3.4 ± 0.7	8 ± 5
XDCPJ0044_08	00:44:05.97	−20:33:16.5	6.0 ± 0.5	22 ± 4
XDCPJ0044_09	00:44:12.80	−20:33:00.5	3.5 ± 0.7	<4
XDCPJ0044_10	00:44:01.13	−20:32:16.5	2.6 ± 0.6	<4
XDCPJ0044_11	00:44:06.82	−20:31:48.5	6.7 ± 0.7	31 ± 5
XDCPJ0044_12	00:44:09.96	−20:31:20.5	4.5 ± 0.9	<4

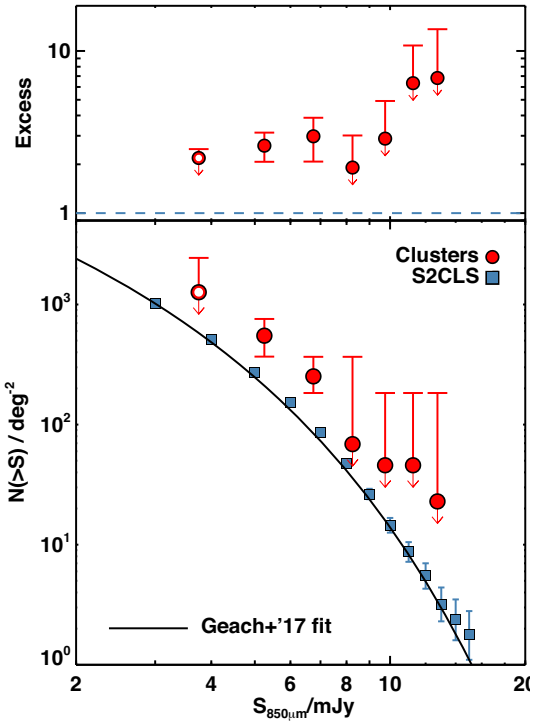

Figure 3. *Bottom:* cumulative number counts for submillimetre sources detected in the central 2.5 arcmin (1.2 Mpc) radius of the cluster fields with observed fluxes $S_{850} \geq 4$ mJy. Fluxes have been deboosted following Geach et al. (2017) and corrected for incompleteness and the expected false-positive rate (13 per cent at $S_{850}^{\rm boosted} \geq 4$ mJy). Error bars show the 16th and 84th percentiles of number densities between individual cluster fields. Upper limits are given where the 16th percentile lower limit includes number densities of zero. The open symbol shows the number counts below our flux limit; there is information here due to the flux deboosting correction. For comparison we also show the number counts from the SCUBA-2 survey of the UDS field. *Top:* cluster counts divided by field counts showing the excess of submillimetre sources in the clusters. Error bars show Poisson errors on the number counts. These $z = 0.8$–1.6 clusters show an overdensity of a factor of 2.8 ± 0.5 relative to the field within their central 2.4 Mpc (diameter).

the fact that an individual source's flux may be overestimated due to noise in the map.[1] Fig. 3 shows the cumulative number counts of 850-μm-selected sources in the cluster fields compared to field counts from the S2CLS/UDS (Geach et al. 2017). In this plot we

[1]We have tested this deboosting correction on each cluster jack-knifed map with our catalogue of fake sources and find the power law derived in Geach et al. (2017) provides a good fit to our data.

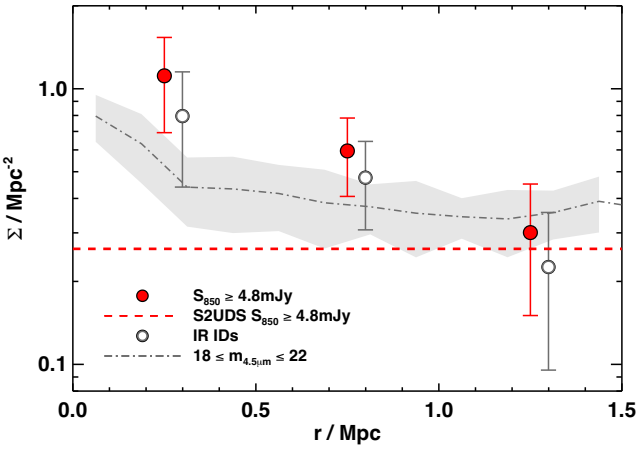

Figure 4. The surface density of 850 μm sources as a function of radius from the cluster X-ray centres. Filled points are all SCUBA-2-selected sources with $S_{850} \geq 4.8$ mJy, which should be compared to the dashed line, which shows the expected field density. We also plot the surface density of the infrared-identified SMG candidate counterparts, the majority of which are expected to lie in the clusters. The points are offset slightly for clarity. Error bars show Poisson errors on the total number of cluster members in each bin. The dot–dashed line shows the median density of IRAC-detected sources with $18 \leq m_{4.5\mu m} \leq 22$, arbitrarily scaled to match the SMG data points. The density of SMGs increases towards the X-ray centre of the clusters, with an overdensity above the field value of 4 ± 2 within the central 1 Mpc diameter.

only use sources in our sample with observed $S_{850} \geq 4$ mJy, where our sample is uniformly selected.

As shown in Fig. 3, over a 5 arcmin diameter field, there is an excess of submillimetre sources in the clusters of 2.8 ± 0.5 times the expected field count down to an observed flux of $S_{850} \geq 4$ mJy. This is a lower overdensity than in other studies of submillimetre sources in high-redshift clusters (e.g. Chapman et al. 2009; Ma et al. 2015); however, we note that there was no pre-selection on star formation activity in our cluster sample.

Since field SMGs are known to be clustered (e.g. Wilkinson et al. 2017), to test the significance of this excess, we repeatedly select eight random regions of 5 arcmin diameter within the S2CLS UDS (Geach et al. 2017) field survey (simulating our sample of eight clusters). We find this average overdensity (0.50 ± 0.05) per cent of the time, indicating our clusters are statistically overdense in terms of submillimetre sources, even compared to the variance in the field.

To investigate the location of submillimetre sources within the clusters, in Fig. 4 we plot the excess of submillimetre sources as a function of cluster-centric radius with respect to the X-ray-detected cluster core. Although our flux cut corresponds to a false detection rate of 13 per cent, the majority of false detections are expected to lie towards the edges of the SCUBA-2 maps, which may bias any radial trends. We thus take a higher and more conservative flux cut of $S_{850} \geq 4.8$ mJy, where we expect zero false detections (Fig. 2), in order to examine the radial trends. Fig. 4 shows that on average the density of submillimetre sources increases towards the X-ray centre of the clusters, with an overdensity above the field value of 4 ± 2 within a 0.5 Mpc radius. The overdensity rapidly drops at larger radii to the field density at $\gtrsim$1 Mpc. This shows that the overdensity of submillimetre sources in our cluster sample is primarily within the central ∼1 Mpc of the clusters. Integrating over all eight clusters we estimate an excess population of $\simeq 28 \pm 6$ sources above the field, most of which are within ∼1 Mpc.

3 PROPERTIES OF SUBMILLIMETRE GALAXIES

We find an excess of submillimetre sources in $z \sim 1$ clusters compared to the field. This excess is on average concentrated within the central 1 Mpc of the cluster cores. In this section we discuss the identification of the galaxies responsible for these submillimetre sources using mid-infrared data.

3.1 Mid-infrared identifications

The SCUBA-2 850 μm effective beam FWHM is $\theta = 14.6$ arcsec, making associations to higher-resolution data at shorter wavelengths difficult. We thus use higher-resolution infrared images from *Spitzer*/MIPS at 24 μm (6 arcsec FWHM) and *Herschel*/PACS at 70 μm and 100 μm (5.2 arcsec and 7.7 arcsec FWHM, respectively), as well as our SCUBA-2 450 μm data (7.5 arcsec FWHM), to identify probable counterparts to the submillimetre sources and obtain their infrared properties. All eight clusters have *Spitzer*/IRAC 3.6 μm and 4.5 μm coverage, seven also have coverage from IRAC 5.8 μm and 8.0 μm, four are covered at 24 μm, and six have either 70 μm or 100 μm data. Only one cluster does not have either 24 μm or 70/100 μm coverage: RCDS J1252.

To identify counterparts, we create catalogues of infrared sources using SExtractor (Bertin & Arnouts 1996) on the *Spitzer*/IRAC 4.5 μm images and measuring fluxes at the resulting positions at 24, 70, 100, and 450 μm, where available. Some example mid-infrared thumbnails for three submillimetre sources are shown in Fig. 5. We then calculate a corrected Poissonian probability p-value (Downes et al. 1986; Dunlop et al. 1989) for all 24, 70, and 100 μm-detected sources within the SCUBA-2 cluster maps.

The probability that a given infrared source is associated with an 850 μm source is a function of magnitude and separation. For each infrared/submillimetre source pairing,

$$P^* = \pi r^2 N_{m<M}, \tag{2}$$

where r is the offset between the infrared and submillimetre sources and $N_{m<M}$ is the number density of infrared sources in the field that have a magnitude m brighter than the magnitude of the infrared source, M. Given a value of P^*, we can derive the probability that the infrared source is a chance alignment with the 850 μm source, $p = (1 - \exp[-E])$, where E is given by

$$\begin{aligned} E &= P^* \qquad P^* > P_c \\ E &= P^*(1 + \log[P_c/P^*]) \qquad P^* \leq P_c. \end{aligned} \tag{3}$$

P_c is the critical Poisson probability level, $P_c = \pi r_s^2 N_T$, where N_T is the total surface density of all detected infrared sources and r_s is the search radius (here we use 7.3 arcsec, the half width at half-maximum of the SCUBA-2 850 μm beam). We identify infrared counterparts to submillimetre sources (Fig. 5) if their p-value is $p \leq 0.05$, based on the results from Hodge et al. (2013) (see also An et al. 2018). We select 23 infrared counterparts to 15/83 submillimetre sources. The colour–magnitude diagram for these candidate counterparts is shown in Fig. 6.

The cluster RCDS J1252 has no coverage by MIPS or PACS. We thus use the IRAC properties of the infrared counterpart SMGs in the other clusters to determine probable IRAC counterparts in RCDS J1252. We use the 3.6 μm and 5.8 μm fluxes from a $0.8 < z < 1.6$ field sample from the UKIDSS/UDS (Almaini et al., in preparation) and $0.8 < z < 1.6$ SMGs from the ALMA/SCUBA-2 UDS survey (AS2UDS; Stach et al. 2018, 2019) plotted in Fig. 6 to determine an infrared colour/magnitude selection for likely $z \sim$ 0.8–1.6 SMGs. Following An et al. (2018), we apply a linear support vector classification using the Python package scikit-learn[2]

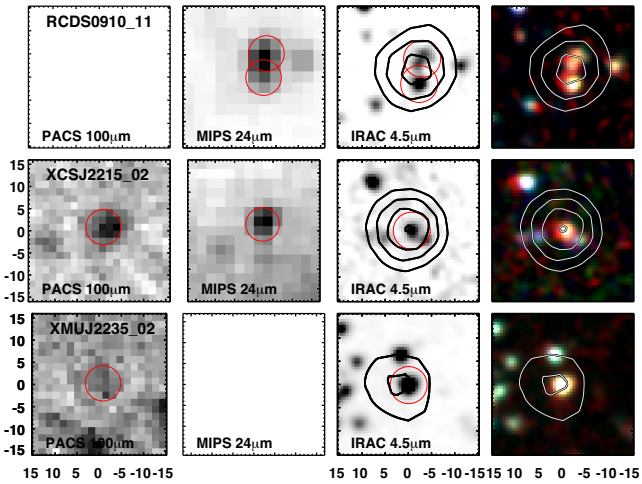

Figure 5. Thumbnails of three example SCUBA-2 detections showing their infrared counterparts at 100, 24, and 4.5 μm, as well as their three-colour 3.6, 4.5, 8.0 μm image. Contours mark the 850 μm detections, starting at 3σ and increasing in steps of 2σ. Red circles outline the positions of infrared counterparts with $p < 0.05$. *Top:* a bright SCUBA-2 source that resolves into two infrared counterparts, both with $p \leq 0.05$, selected at 24 μm and visible at 4.5 μm. *Middle:* a SCUBA-2 source with a single infrared counterpart with $p \leq 0.05$, detected at all wavelengths. *Bottom:* an example of a source undetected at 100 μm, but selected by its IRAC colour with $p \leq 0.05$.

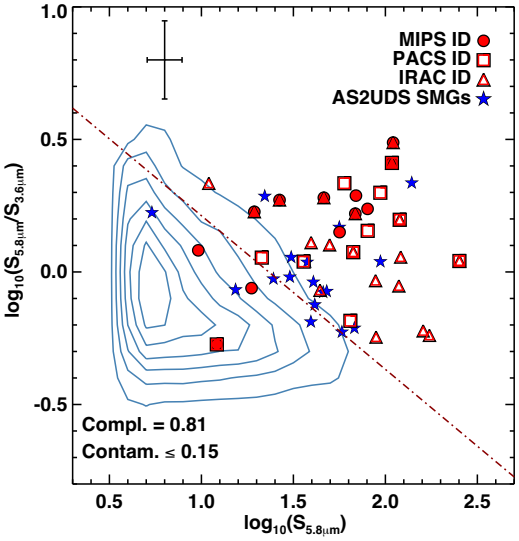

Figure 6. The *Spitzer*/IRAC properties of infrared counterparts to SCUBA-2 850 μm sources in our cluster survey. The contours show the distribution of field galaxies in the UKIDSS Ultra Deep Survey (UDS) field (Almaini et al., in preparation). The dot–dashed line shows the scikit learn-derived separation between $z \sim 0.8$–1.6 AS2UDS SMGs (Stach et al. 2019) and field galaxies, used to select IRAC counterparts to 850 μm sources with no MIPS or PACS coverage. This shows that using this selection and a matching probability $p \leq 0.05$ results in a sample with similar properties to those of known SMGs. A typical error bar for the candidate SMG counterparts is shown in the top left.

[2]http://scikit-learn.org

(Pedregosa et al. 2011) to derive the optimal SMG selection:

$$\log_{10}(S_{5.8}/S_{3.6}) > 1.099 - 0.835 \times \log_{10}(S_{5.8}). \quad (4)$$

We then select as SMG counterparts any sources that satisfy equation 4 ('IRAC colour-selected sources') and have p-values (using the 3.6 μm magnitudes) $p \leq 0.05$. We find 19 IRAC colour-selected counterparts, 9 of which also have a 24 μm and/or a 70/100 μm detection. We test this method by randomizing the positions of all IRAC colour-selected sources in each cluster field and remeasuring their p-values. We select a source with $p \leq 0.05$ in five per cent of the randomizations. We therefore expect to find one IRAC colour-selected counterpart to four SCUBA-2 sources due to random alignments, compared to the 19 candidate counterparts that we identify. This is an upper limit at it does not take into account any additional information from 24 μm, 70 μm, or 100 μm detections.

Hodge et al. (2013) showed that by using mid-infrared detections, counterparts to single-dish submillimetre sources are correct in 80 per cent of cases, but are only recovered in 45 per cent of submillimetre sources. We identify counterparts to 33 per cent (26/83) of the submillimetre sources in our sample, which is consistent with the findings of Hodge et al. (2013) and our estimate of the likely number of 850 μm sources that are associated with the cluster overdensities in Section 2.2. Our cluster sample is at a lower redshift than the average of the sample from Hodge et al. (2013) ($z \sim 2.5$; da Cunha et al. 2015), meaning the K-correction at 24 μm and 70/100 μm is smaller and thus making it easier to detect mid-infrared counterparts that are candidate cluster members. We therefore expect our counterparts to be $\gtrsim$80 per cent accurate.

To summarize, we select SMGs as any sources with $p \leq 0.05$ that have a 24 μm counterpart and/or a 70/100 μm counterpart and/or an IRAC colour-selected source. Table 3 lists the properties of all the infrared counterpart SMGs as well as the method used to identify them. In total we find 26/83 SCUBA-2 sources have at least one infrared-selected counterpart, with 34 infrared-selected SMGs in total from the 26 SCUBA-2 sources. 19/83 SCUBA-2 sources have IRAC colour-selected counterparts, 9 of which also have a 24 μm and/or a 70/100 μm detection. 9/83 and 9/83 sources have 24μm- and 70/100μm-selected counterparts, respectively.

57/83 SCUBA-2 sources do not have any infrared counterpart assigned to them. This gives a (completeness-corrected) number density of $\sim$1300 deg^{-2} for the SCUBA-2 sources brighter than 4 mJy that lack counterparts, consistent with the expected surface density of the field population (Fig. 3), which are typically at higher redshifts ($z \sim 2.5$; Danielson et al. 2017; Stach et al. 2019). These sources are probably background field SMGs and not cluster members, although spectroscopic redshift information is required to confirm this.

Of our 34 infrared-selected SMGs, we expect the majority to be cluster members due to the smaller K-correction in the infrared at $z \sim 0.8$–1.6, compared to the average redshift of SMGs ($z \sim 2.5$). Future spectroscopic observations of these targets will be able to confirm their cluster membership, and constrain their relative velocities within the cluster.

We find that 7/26 submillimetre sources that have robust infrared identifications have more than one counterpart with $p \leq 0.05$. If all of these counterparts are SMGs, this suggests a multiplicity rate for the single-dish sources of 30 ± 10 per cent. This is slightly higher than the rate in field surveys, which have a multiple fraction of $\gtrsim$15 per cent for $S_{850} \geq 3.5$ mJy (Stach et al. 2018). However, we stress that to reliably identify SMG counterparts to submillimetre sources higher-resolution submillimetre observations, such as from ALMA or the Sub-Millimeter Array, are crucial. This is particularly true for crowded fields such as the cluster cores in this sample, as the density of potential counterparts is much higher. Indeed, Stach et al. (2017) used ALMA observations to resolve four single-dish submillimetre sources into 14 separate SMGs in the core of XCS J2215.

3.2 Testing cluster membership

Most of the clusters in this study have spectroscopic coverage in the optical or near-infrared. We have searched for any archival spectroscopic redshifts for our candidate cluster members and find two matches: RX J0849_02a and XCS J2215_06a. The archival redshift for RX J0849_02a places it at $z = 1.589$, which indicates that this is a background source and not a cluster member. The source in XCS J2215 is a spectroscopically confirmed cluster member (Stach et al. 2017). We also note that there are a further 11 spectroscopically confirmed, submillimetre-detected cluster members from Stach et al. (2017) and Hayashi et al. (2017) that are not selected in our sample because they have $S_{850} < 4$ mJy. To confirm the membership of our sample, future deep near-infrared or submillimetre spectroscopy is required.

Due to the negative K-correction at submillimetre wavelengths, the ratio of 24 μm flux density to 850 μm flux density is expected to decrease towards higher redshifts (e.g. Cowie et al. 2018). Four of the eight clusters have MIPS 24 μm coverage sensitive enough to detect flux ratios down to $S_{24}/S_{850} \sim 0.02$. Within these four clusters, 12 sources have an MIPS identification with $p \leq 0.05$ and a further 13 have measurable 24 μm fluxes (Table 3). In Fig. 7 we plot the evolution of the 24 μm/850 μm flux ratio with redshift for SMGs from the AS2UDS survey (Stach et al. 2019) and from the GOODS-S field (Cowie et al. 2018) and compare it to those for our sample of four clusters. The cluster sample on average has 24 μm/850 μm flux consistent with the field at $1 \lesssim z \lesssim 1.5$, albeit with a large scatter between potential cluster members. This is further evidence that by selecting submillimetre sources with infrared counterparts, we are selecting probable cluster member SMGs rather than background sources.

The SMGs in RX J0152 at $z = 0.83$ have a median S_{24}/S_{850} ratio a factor of 2 lower than the field SMG population at $z \sim 0.8$. This cluster has been extensively studied and has been shown to have an irregular structure and a strongly lensing core. We discuss RX J0152 further in Section 4.2. The lower flux ratios, however, may indicate that some of the SMGs we observe in this cluster field are lensed background galaxies, with colours more consistent with $2 < z < 3$ SMGs.

4 RESULTS AND DISCUSSION

4.1 Radial overdensity

In local clusters, star-forming galaxies are preferentially located on the outskirts of these massive structures, whereas the core is populated by passive galaxies (e.g. von der Linden et al. 2010; Peng et al. 2010). The location of star-forming members provides indicators for the formation and quenching mechanisms of cluster galaxies. For example, galaxies falling into the dense intra-cluster medium may have their cold gas stripped and thus cease forming stars (e.g. Gunn & Gott 1972; Jaffé et al. 2018). Conversely, interactions and mergers between gas-rich galaxies may cause starburst events (e.g. Mihos & Hernquist 1994; Kocevski et al. 2011).

Table 3. Table of identifications and infrared properties of SCUBA-2-identified submillimetre sources with infrared counterparts.

ID	IR RA [J2000]	IR Dec. [J2000]	Counterpart selection MIPS	PACS	IRAC	$S_{3.6}$ [μJy]	$S_{4.5}$ [μJy]	$S_{5.8}$ [μJy]	$S_{8.0}$ [μJy]	S_{24} [mJy]	$S^{1}_{\rm PACS}$ [mJy]
RXJ0152_01a	01:52:43.83	– 13:58:56.4	1	0	0	40 ± 10	50 ± 10	60 ± 10	70 ± 20	0.82 ± 0.04	5.37 ± 0.09
RXJ0152_01b	01:52:44.12	– 13:58:52.3	1	0	1	24 ± 8	30 ± 9	50 ± 10	40 ± 10	0.49 ± 0.03	...
RXJ0152_03a	01:52:42.16	– 13:58:08.1	0	1	0	28 ± 9	40 ± 10	60 ± 10	60 ± 10	0.50 ± 0.03	11.05 ± 0.09
RXJ0152_03b	01:52:42.04	– 13:58:02.7	1	1	0	23 ± 8	22 ± 8	12 ± 7	11 ± 7	0.44 ± 0.03	6.36 ± 0.09
RXJ0152_07a	01:52:40.14	– 13:57:09.6	1	0	1	11 ± 6	17 ± 7	19 ± 8	21 ± 9	0.11 ± 0.02	...
RXJ0152_10a	01:52:32.98	– 13:57:07.4	0	1	0	19 ± 7	22 ± 8	21 ± 8	22 ± 9	0.34 ± 0.03	5.12 ± 0.09
RXJ0152_10b	01:52:32.85	– 13:57:03.4	0	1	0	60 ± 10	70 ± 10	80 ± 20	70 ± 20	0.34 ± 0.03	5.90 ± 0.10
RXJ0152_13a	01:52:41.11	– 13:55:56.2	1	0	1	40 ± 10	60 ± 10	70 ± 10	60 ± 10	0.55 ± 0.03	...
WARP1415_01a	14:15:10.82	+36:11:00.1	0	0	1	50 ± 10	50 ± 10	40 ± 10	50 ± 10	...	...
WARP1415_07a	14:15:13.47	+36:12:10.9	0	0	1	300 ± 30	260 ± 30	170 ± 20	180 ± 20	...	...
WARP1415_10a	14:15:11.42	+36:13:05.1	0	0	1	31 ± 9	40 ± 10	40 ± 10	30 ± 10	...	...
RCDS0910_01a	09:10:40.93	+54:20:41.5	1	0	1	14 ± 6	17 ± 7	27 ± 10	2 ± 5	0.41 ± 0.03	...
RCDS0910_01b	09:10:40.69	+54:20:45.0	1	0	0	22 ± 8	27 ± 9	19 ± 8	3 ± 5	0.50 ± 0.04	...
RCDS0910_04a	09:10:45.48	+54:21:22.3	0	0	1	5 ± 4	4 ± 4	11 ± 7	30 ± 10	0.07 ± 0.02	...
RCDS0910_11a	09:10:54.86	+54:22:18.1	1	0	0	50 ± 10	60 ± 10	80 ± 20	110 ± 20	1.32 ± 0.05	...
RCDS0910_11b	09:10:54.79	+54:22:23.5	1	0	0	36 ± 10	50 ± 10	70 ± 10	60 ± 10	1.47 ± 0.05	...
RCDS1252_02a	12:52:47.83	– 29:27:52.9	0	0	1	40 ± 10	50 ± 10	50 ± 10	40 ± 10	...	...
RCDS1252_08a	12:53:00.99	– 29:25:40.7	0	0	1	160 ± 20	120 ± 20	90 ± 20	60 ± 10	...	...
RXJ0849_02a[2]	08:48:58.59	+44:52:30.3	0	0	1	270 ± 30	220 ± 20	160 ± 20	140 ± 20	0.32 ± 0.03	...
RXJ0849_04a	08:49:07.62	+44:53:50.1	1	0	1	36 ± 10	60 ± 10	110 ± 20	220 ± 30	0.56 ± 0.04	...
XMUJ2235_02a	22:35:21.48	– 25:56:58.5	0	0	1	110 ± 20	130 ± 20	120 ± 20	80 ± 20	...	...
XMUJ2235_03a	22:35:15.45	– 25:57:02.9	0	1	1	60 ± 10	70 ± 10	70 ± 10	60 ± 10	...	4.26 ± 0.07
XCSJ2215_01a	22:16:01.19	– 17:39:35.4	0	1	1	80 ± 10	70 ± 10	120 ± 20	160 ± 20	0.80 ± 0.10	5.03 ± 0.06
XCSJ2215_02a	22:15:59.01	– 17:39:42.6	1	1	1	40 ± 10	60 ± 10	110 ± 20	150 ± 20	0.67 ± 0.10	9.43 ± 0.06
XCSJ2215_03a	22:16:02.73	– 17:38:39.2	0	1	0	...	12 ± 6	3 ± 4	6 ± 7	1.28 ± 0.09	17.34 ± 0.06
XCSJ2215_03b	22:16:03.03	– 17:38:36.8	0	1	0	50 ± 10	60 ± 10	90 ± 20	90 ± 20	1.29 ± 0.09	22.28 ± 0.06
XCSJ2215_03c	22:16:03.16	– 17:38:39.8	0	1	1	230 ± 20	230 ± 30	250 ± 30	360 ± 30	1.27 ± 0.08	27.51 ± 0.06
XCSJ2215_04a	22:16:00.56	– 17:38:35.4	0	0	1	100 ± 20	110 ± 20	90 ± 20	50 ± 10	0.84 ± 0.07	4.65 ± 0.06
XCSJ2215_06a[3]	22:15:59.71	– 17:37:59.0	0	0	1	130 ± 20	170 ± 20	120 ± 20	100 ± 20	0.51 ± 0.07	4.46 ± 0.06
XCSJ2215_07a	22:16:04.75	– 17:37:51.9	0	1	0	33 ± 9	40 ± 10	40 ± 10	30 ± 10	0.25 ± 0.08	8.91 ± 0.07
XCSJ2215_07b	22:16:04.97	– 17:37:54.3	0	1	0	100 ± 20	70 ± 10	60 ± 10	60 ± 10	0.28 ± 0.09	8.23 ± 0.07
XCSJ2215_09a	22:15:59.99	– 17:37:18.2	1	0	0	8 ± 5	8 ± 5	10 ± 6	4 ± 5	2.10 ± 0.20	...
XDCPJ0044_01a	00:44:06.17	– 20:34:38.7	0	1	0	480 ± 40	490 ± 40	...	...	...	45.19 ± 0.09
XDCPJ0044_11a	00:44:06.81	– 20:31:47.2	0	1	0	60 ± 10	70 ± 10	...	...	...	7.80 ± 0.10

Notes. [1]PACS data for RX J0152−1357 and RX J0849+4453 are at 70 μm. The other fields are covered by 100 μm data.
[2]Archival spectroscopic data for this source suggests a redshift of $z = 1.589$, suggesting it is not a cluster member (Albareti et al. 2017).
[3]Confirmed cluster member (Stach et al. 2017).

Using 24 μm and 70/100 μm counterparts we expect to predominantly select SMG members of the $z \sim 1$ clusters, rather than background interlopers. In Fig. 4 we showed that the density of submillimetre sources increases towards the X-ray-defined centre of the clusters, with an overdensity above the field value of 4 ± 2 within 1 Mpc. We also show SMGs for which we identify infrared counterparts. The infrared counterparts follow the same overall trend as the submillimetre detections, although with lower significance.

The increase in density of our candidate SMGs near the X-ray centre of the clusters suggests that the candidate cluster SMGs lie within the central ∼500 kpc of the structures. The short gas-consumption time-scale of SMGs (typically 10^7–10^8 yr; Bothwell et al. 2013) means that they are unlikely to have moved far from the environment where the intense star formation event began (∼0.01–0.1 Mpc, assuming a velocity of 1000 km s^{-1}). This means that the star formation event was likely triggered within the central ∼1 Mpc core of these massive clusters.

A number of studies have suggested that the triggering mechanism for SMGs may be interactions or mergers (e.g. Swinbank et al. 2006; Ivison et al. 2007; Engel et al. 2010; Chen et al. 2015). The overdensity of dust-obscured star formation within the cores of these $z \sim 1$ clusters therefore may suggest an overdensity of gas-rich mergers between cluster members at radii <500 kpc.

4.2 Total cluster star formation rates

Although in the local Universe there is a clear trend of lower star formation rates in denser environments (e.g, Kauffmann et al. 2004), at higher redshifts there are indications that this trend reverses at the epoch of cluster galaxy formation (e.g. Elbaz et al. 2007; Tran et al. 2010; Elbaz et al. 2011; Brodwin et al. 2013, but see also Quadri et al. 2012; Ziparo et al. 2014; Muldrew, Hatch & Cooke 2018). In addition, previous studies of individual clusters suggested a rapid evolution in the mass-normalized star formation rate of $\propto (1 + z)^{\gamma}$, with $\gamma = 6$–7 (e.g. Kodama et al. 2004; Geach et al. 2006; Koyama et al. 2010, 2011; Shimakawa et al. 2014; Smail et al. 2014), compared to $\gamma = 3$–4 for field galaxies (e.g. Ilbert et al. 2015). Here we examine the mass-normalized total star formation rate of our cluster candidate sample compared to lower-redshift results.

To calculate cluster masses we use their X-ray temperatures ($T_{\rm X}$) from the literature (Table 1; Stanford et al. 2001, 2002; Maughan

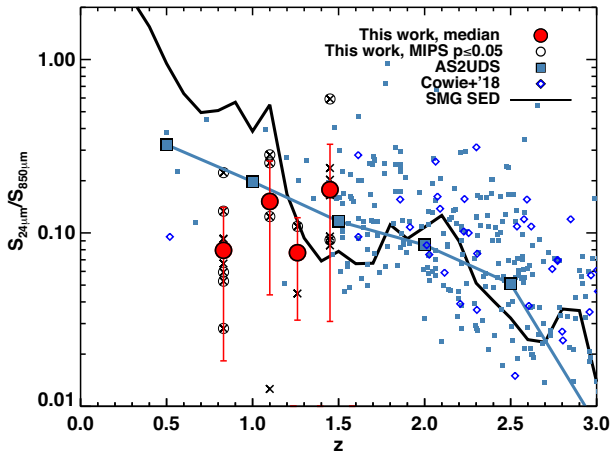

Figure 7. The evolution of the S_{850}/S_{24} flux ratio with redshift for our cluster SMGs and samples of field SMGs from AS2UDS (Stach et al. 2018; Dudzevičiūtė et al., in preparation) and GOODS-S (Cowie et al. 2018). Where MIPS coverage is available, all SMGs are detected at 24 μm. Small black crosses without circles have been selected via their 70/100 μm or IRAC colour. We plot the median and scatter for individual clusters and the median field flux ratio in redshift bins. The black solid line is a composite SMG SED (Swinbank et al. 2014). Albeit with large scatter between potential cluster members, overall cluster SMGs appear to have similar colours to field SMGs. The SMGs in RX J0152 at $z = 0.83$ have a median ratio a factor of 2 lower than the general SMG population at $z \simeq 0.8$, which may indicate contamination from higher-redshift SMGs.

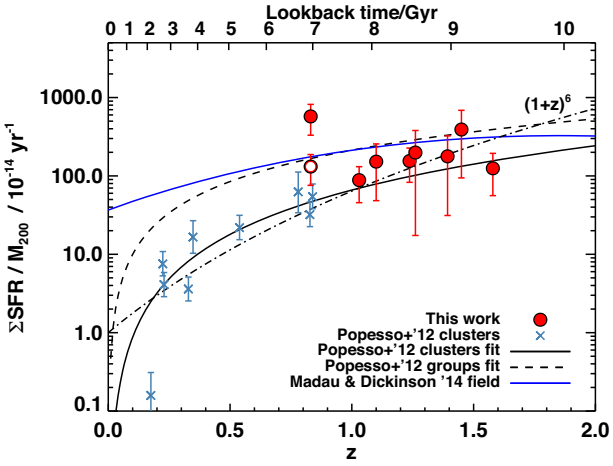

Figure 8. The total star formation rate per cluster mass (M_{200}) as a function of redshift. The small blue points and lines show previous work at $z < 1$ (Popesso et al. 2012). The open symbol shows the value of RX J0152 if we use the cluster mass from Popesso et al. (2012). The ratio is still higher than their value due to our measured higher star formation rate, which may be contaminated by background sources (see Section 3.2). The submillimetre star formation rates of the cluster sample are consistent with a continuation of the lower-redshift trend within the scatter, but can also be fitted by a steeper relation $\sim(1+z)^6$.

et al. 2003; Rosati et al. 2004; Mullis et al. 2005; Stanford et al. 2006; Branchesi et al. 2007; Tozzi et al. 2015) and the relation between T_X and M_{500} from Kettula et al. (2013). We then convert to M_{200} assuming the density profile from Navarro, Frenk & White (1996) with a concentration value of 5 (Bullock et al. 2001). Star formation rates were calculated using a conversion between the measured 850 μm flux and star formation rate:

$$\log_{10}(\mathrm{SFR}) = (0.87 \pm 0.06) \times \log_{10}(S_{850}) + (1.85 \pm 0.04) \quad (5)$$

calculated from fitting the star formation rate derived using MAGPHYS (da Cunha, Charlot & Elbaz 2008) on the full spectral energy distribution for the 45 SMGs at $z_{\mathrm{phot}} = 0.8$–1.6 drawn from a full sample of over 700 SMGs in the AS2UDS survey (Stach et al. 2018, 2019; Dudzevičiūtė et al., in preparation). This scaling relation is derived between observed 850 μm flux and far-infrared-derived star formation rate and has a dispersion of 0.27 dex.

Fig. 8 shows the integrated star formation rate normalized by cluster mass. We see that our clusters at $z = 0.8$–1.6 are consistent with the overall trend of higher mass-normalized star formation rate at higher redshifts. Our sample is consistent with a continuation of the trend found in Popesso et al. (2012) or the $\sim(1+z)^6$ evolution suggested by intermediate-redshift studies of Hα emitters (e.g. Kodama et al. 2004; Koyama et al. 2010, 2011). Our current data are unable to distinguish between these trends.

One of the clusters in this work, RX J0152, was also studied by Popesso et al. (2012). We find an integrated star formation rate to cluster mass ratio a factor of 16 times larger than that study. This is due to both a factor of 4 times lower cluster mass estimate and the factor of 4 times higher measured star formation rates in our study. Popesso et al. (2012) measured cluster masses using cluster members' velocity dispersions, whereas we convert the X-ray temperature as above. In Fig. 8 we show as an open symbol the value if we instead adopt the cluster mass listed in Popesso et al. (2012). In addition, our measured star formation rates are higher than those listed in Popesso et al. (2012). This may indicate that the large effective beam of SCUBA-2 means that the 850 μm flux measurements are potentially contaminated by background sources, boosting the measured star formation rates. The data points in Fig. 8 may therefore be considered upper limits; however, we note that we have taken a conservative flux cut and thus may also be missing fainter cluster members, which would increase the total star formation rates.

Previous studies of RX J0152 have revealed a double-core system, indicative of an early-stage cluster-to-cluster merger (e.g. Rosati et al. 1998; Maughan et al. 2003; Tanaka et al. 2006). The central regions of RX J0152 are also known to be forming strong lensing multiple images of background systems (Umetsu et al. 2005; Acebron et al. 2019). None of our submillimetre sources are identified as lensed by recent strong lensing studies (Acebron et al. 2019); however, if some of the detected submillimetre sources in the cluster are actually lensed background sources, then this may increase our measured star formation rate, and may explain the lower S_{24}/S_{850} ratios in Section 3.2. Further spectroscopic observations are required to determine the cluster membership of the observed SMGs. However, we note that if we remove RX J0152 from our sample none of our results change qualitatively.

In Fig. 4 we showed that the overdensity of SMGs in our cluster sample is strongest within the central 0.5 Mpc. Two clusters in our sample, XCS J2215 and RX J0152 (at $z = 1.45$ and $z = 0.83$, respectively), have bimodal cores, indicating they are likely undergoing a cluster-to-cluster merger (Maughan et al. 2003; Stanford et al. 2006; Hilton et al. 2010). In Fig. 8, XCS J2215 and RX J0152 are the clusters with the highest star formation rate densities. This may be hinting that cluster-to-cluster mergers may be responsible for triggering extreme star formation activity within the resulting system's core.

We now examine whether the overdensity of star-forming galaxies in the cores of these clusters indicates a reversal in the local star-formation-rate–density relation. The median normalized star formation rate for the central ∼2.5 Mpc of the $z = 0.8$–1.6 clusters[3] is $\Sigma\mathrm{SFR}/M_{\mathrm{cl}} = 180^{+20}_{-50} \times 10^{-14}\,\mathrm{yr}^{-1}$. To calculate the equivalent value for field galaxies we follow Popesso et al. (2012) and adopt the cosmic star formation rate density from Madau & Dickinson (2014) and divide it by the mean comoving density of the Universe ($\Omega_{\mathrm{M}} \times \rho_{\mathrm{crit}}$, where ρ_{crit} is the critical density of the Universe) to get $\mathrm{SFR}/M = 270^{+30}_{-60} \times 10^{-14}\,\mathrm{yr}^{-1}$. The normalised star-formation rate for the candidate cluster sample is lower than the field by a factor of 1.5 ± 0.3. This suggests that there is no evidence for a systematic reversal in the star-formation-rate–density relation on 2.5 Mpc scales up to $z = 1.6$; however, we note that we have taken conservative flux cuts for our SMG sample. ALMA observations of XCS J2215 revealed 14 SMGs within the central 500 kpc of the cluster core (Hayashi et al. 2017; Stach et al. 2017). Future deep observations to select fainter submillimetre sources and spectral analysis to confirm their cluster membership may uncover more SMGs and thus higher total star formation rates within these cluster cores.

4.3 Future evolution

SMGs have been suggested as the progenitors of local spheroidal galaxies. We therefore examine the future evolution of our cluster candidate sample to see whether its luminosity distribution is consistent with local passive cluster galaxies. To 'evolve' our population to $z = 0$ we follow the method of Simpson et al. (2014) and calculate the expected change in rest-frame H-band magnitude (observed-frame 3.6–4.5 μm) from $z \sim 1.2$[4] to $z = 0$. This method uses Bruzual & Charlot (2003) simple stellar population models to determine the H-band luminosity halfway through a 100 Myr burst (taken as the typical lifetime of an SMG) at $z \sim 1$ and predict its evolution to the present day. We also run these models with 50 Myr and 200 Myr bursts and show the offset in H-band magnitude for these as vectors in Fig. 9. This is a simple model and assumes that the pre-burst stellar population's luminosity contribution is negligible and that each SMG only goes through a single burst phase and does not subsequently accrete significant stellar mass through dry mergers. Fig. 9 shows the absolute H-band magnitudes of the candidate cluster SMGs, faded to $z = 0.023$, compared to present-day elliptical galaxies in the Coma cluster (Smith et al. 2009; Hainline et al. 2011; R. Smith, private communication). The SMG distribution has a median H-band magnitude of $M_H = -21.5 \pm 0.2$, consistent with that of present-day cluster ellipticals ($M_H = -21.2 \pm 0.3$), suggesting these candidate cluster SMGs could evolve into passive ellipticals by $z = 0$.

To estimate whether the number of SMGs we observe in our cluster sample at $z \sim 1$ is sufficient to explain the observed passive population in clusters at $z = 0$ we estimate the infall rate and duty cycle of the SMG phase to correct our apparent numbers of SMGs in $z \sim 1.2$ clusters to the expected present-day descendants and also add in those galaxies that are already passive at $z \sim 1.2$. To do this we use the implementation of the Bower et al. (2006) galaxy formation recipe in the Millennium Simulation (Springel et al. 2005). We use the most massive halo in the simulation (which has a mass of

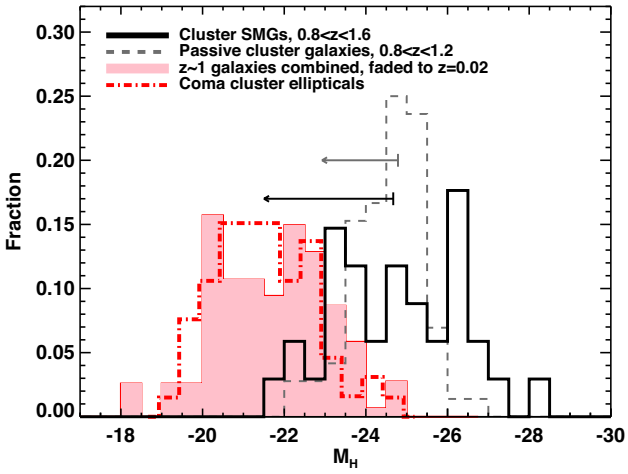

Figure 9. Comparison of the distributions of absolute H-band magnitude for our cluster SMG sample, a spectroscopic $z \sim 1$ passive cluster sample (Muzzin et al. 2009; Demarco et al. 2010) and elliptical galaxies from the Coma cluster. The shaded histogram shows the distribution of the SMGs and passive samples evolved to $z = 0.023$ (shown by the arrows) and combined. For this we assume that the SMG starbursts we observe are 100 Myr in duration and on average we observe the SMGs halfway through the starburst. If we instead consider a 50 Myr or 200 Myr burst, the SMG distribution shifts by +0.06 mag and −0.5 mag, respectively. A two-sided Kolmogorov–Smirnov test comparing the combined sample to the Coma distribution gives $p = 0.7$. The passive population in $z \sim 0$ clusters is consistent with forming at $z \geq 1$ through a series of dusty starbursts.

$\sim 1 \times 10^{14}\,\mathrm{M}_{\odot}$ at $1 \lesssim z \lesssim 2$, roughly matching the expected masses of our cluster sample) and a spherical search radius of 1.5 Mpc, matching our SCUBA-2 survey field. We searched the simulation snapshots between $z = 0.91$ and $z = 1.84$ for galaxies with cold gas masses of $> 1 \times 10^{10}\,\mathrm{M}_{\odot}$ lying within this sphere. We then identify unique entries in the output for each of these gas-rich galaxies, on the expectation that the gas reservoir will be quickly exhausted by the intense star formation events we are searching for. There are a total of 40 such galaxies found over a duration of 2.7 Gyr, with an average of 1.5 ± 0.7 SMGs in any given 100 Myr snapshot. Given that the average SMG phase lasts approximately 100 Myr, this is the expected number of observable SMGs per cluster at these redshifts. The median of our sample is two SMGs per cluster. Thus, our approximation, although crude, is in agreement with our observations. This suggests a correction factor to account for all such submillimetre-bright galaxies accreted on to a typical cluster since $z \sim 2$ of $\sim 25 \pm 7$.

A similar calculation using the average cluster mass growth and stellar mass function taken from Muldrew, Hatch & Cooke (2015) suggests that we would expect to observe 1–3 SMGs per cluster and a correction factor of ∼10. Our estimated correction factor may therefore change by a factor of 2. We have tested our analysis with both correction factors and find our conclusions do not qualitatively differ.

Although the median of our SMG sample is consistent with that of present-day cluster ellipticals, by $z \sim 1$ most clusters already have a population of passive galaxies (e.g. Eisenhardt et al. 2008). In Fig. 9 we therefore combine our SMG sample with a $z \sim 1$ spectroscopic sample from Muzzin et al. (2009) and Demarco et al. (2010). This sample is incomplete at faint magnitudes ($M_H \geq -24$). We have tested the effect this may have on our conclusions by multiplying the faint end of the spectroscopic distribution by a

[3]Including RX J0152 the median is $\Sigma\mathrm{SFR}/M_{\mathrm{cl}} = 200^{+200}_{-60} \times 10^{-14}\,\mathrm{yr}^{-1}$.
[4]We calculate the expected change in H-band magnitude for each cluster individually to account for the different redshifts.

factor of 100 before combining them with the SMG sample. We find that our conclusions do not qualitatively change. We scale the number of SMGs observed by a factor of 25, as calculated above, to account for the duty cycle of the SMG phase, fade them to $z \sim 0$, and then combine the distribution with that of the faded $z \sim 1$ passive galaxies. As shown in Fig. 9, the combined SMG+passive distribution is similar to that of the Coma ellipticals in terms of median luminosity and width; a two-sided Kolmogorov–Smirnov test gives $p = 0.7$. This therefore suggests that the passive population in $z \sim 0$ clusters is consistent with having formed all of its stars at $z \geq 1$ through a series of dusty starbursts.

5 CONCLUSIONS

We have observed a sample of eight massive galaxy clusters at $0.8 < z < 1.6$ with SCUBA-2 at 850 μm. We select 83 submillimetre sources with either S/N ≥ 4 or $S_{850} \geq 4$ mJy within 2.5 arcmin radii of the cluster cores (1.2 Mpc at $z = 1.2$). We find an overdensity of submillimetre sources of a factor of 2.8 ± 0.5 over the expected field density. This overdensity is mostly concentrated within ∼500 kpc around the X-ray-detected cluster cores: a factor of 4 ± 2 overdense within 1 Mpc diameter, suggesting there is ongoing dusty star formation in the centres of massive clusters at $z \sim 1$.

We use higher-resolution infrared images to select likely cluster member SMGs. We match 26 of the low-resolution submillimetre sources to 34 likely infrared counterparts and examine their multiwavelength properties. The remaining 56 submillimetre sources have a number density consistent with the field population and are therefore expected to be background field SMGs at higher redshifts. We find that the total amount of star formation, normalized by cluster mass, increases out to $z \sim 1.5$ and is consistent with a more rapid evolution ($\sim(1+z)^6$) than the $\sim(1+z)^4$ trend from the field. Even with this rapid evolution, the mass-normalized star formation rate for clusters at $1 < z < 1.6$ is lower than the field by a factor of 1.5 ± 0.3. We therefore find no evidence with our current data of a reversal of the local star-formation-rate–density relation in the most massive X-ray-detected clusters at $z \sim 0.8$–1.6.

Finally, we use a simple model to predict the H-band luminosities of our candidate cluster SMGs evolved to the present day and compare this to both local cluster ellipticals and the population of cluster galaxies that are already passive by $z \sim 1$. We find that the evolved distribution of M_H from our star-forming cluster sample is consistent with that of faint ($M_H \gtrsim -22$) passive elliptical galaxies in the Coma cluster. Combining the passive cluster population at $z \sim 1$ with the SMG sample, we can reproduce the expected cluster population at $z = 0$. This suggests that the majority of the passive population in $z \sim 0$ clusters is consistent with having formed at $z \gtrsim 1$–1.5 through an extreme, dust-obscured starburst event.

ACKNOWLEDGEMENTS

The authors would like to thank the anonymous referee for their comments which improved the flow and content of this paper. The authors would also like to thank the following people for useful discussions and help with the survey: James Simpson, Renske Smit, C. J. Ma, Alex Karim, John Stott, Ken Tadaki, Masayuki Tanaka, Simona Mei, and John Blakeslee. EAC and IRS acknowledge support from the ERC Advanced Investigator Grant DUSTYGAL (321334) and STFC (ST/P000541/1). We also acknowledge STFC support to the UK consortium members of EAO (ST/M007634/1, ST/M003019/1and ST/N005856/1). APT acknowledges support from STFC (ST/P000649/1).

This work makes use of data from JCMT project IDs M13AU029, M13BU010, M15BI006, M16AP053, and M16BP080. The James Clerk Maxwell Telescope is operated by the East Asian Observatory on behalf of The National Astronomical Observatory of Japan; Academia Sinica Institute of Astronomy and Astrophysics; the Korea Astronomy and Space Science Institute; the Operation, Maintenance and Upgrading Fund for Astronomical Telescopes and Facility Instruments, budgeted from the Ministry of Finance (MOF) of China and administrated by the Chinese Academy of Sciences (CAS), as well as the National Key R&D Program of China (No. 2017YFA0402700). Additional funding support is provided by the Science and Technology Facilities Council of the United Kingdom and participating universities in the United Kingdom and Canada.

This work is based in part on archival data obtained with the *Spitzer Space Telescope* and the NASA/IPAC Extragalactic Database (NED), which are operated by the Jet Propulsion Laboratory, California Institute of Technology under a contract with the National Aeronautics and Space Administration. This research also used the facilities of the Canadian Astronomy Data Centre operated by the National Research Council of Canada with the support of the Canadian Space Agency.

REFERENCES

Acebron A. et al., 2019, ApJ, 874, 132
Albareti F. D. et al., 2017, ApJS, 233, 25
Alberts S. et al., 2014, MNRAS, 437, 437
An F. X. et al., 2018, ApJ, 862, 101
Bamford S. P. et al., 2009, MNRAS, 393, 1324
Bertin E., Arnouts S., 1996, A&AS, 117, 393
Best P. N., 2002, MNRAS, 336, 1293
Bothwell M. S. et al., 2013, MNRAS, 429, 3047
Bower R. G., Lucey J. R., Ellis R. S., 1992, MNRAS, 254, 601
Bower R. G., Benson A. J., Malbon R., Helly J. C., Frenk C. S., Baugh C. M., Cole S., Lacey C. G., 2006, MNRAS, 370, 645
Branchesi M., Gioia I. M., Fanti C., Fanti R., 2007, A&A, 472, 739
Brodwin M. et al., 2013, ApJ, 779, 138
Bruzual G., Charlot S., 2003, MNRAS, 344, 1000
Bullock J. S., Kolatt T. S., Sigad Y., Somerville R. S., Kravtsov A. V., Klypin A. A., Primack J. R., Dekel A., 2001, MNRAS, 321, 559
Cerulo P. et al., 2016, MNRAS, 457, 2209
Chapin E. L., Berry D. S., Gibb A. G., Jenness T., Scott D., Tilanus R. P. J., Economou F., Holland W. S., 2013, MNRAS, 430, 2545
Chapman S. C., Blain A., Ibata R., Ivison R. J., Smail I., Morrison G., 2009, ApJ, 691, 560
Chen C.-C. et al., 2015, ApJ, 799, 194
Chen C.-C., Cowie L. L., Barger A. J., Casey C. M., Lee N., Sanders D. B., Wang W.-H., Williams J. P., 2013, ApJ, 776, 131
Citro A., Pozzetti L., Moresco M., Cimatti A., 2016, A&A, 592, A19
Cooke E. A. et al., 2015, MNRAS, 452, 2318
Cooke E. A. et al., 2016, ApJ, 816, 83
Cowie L. L., González-López J., Barger A. J., Bauer F. E., Hsu L.-Y., Wang W.-H., 2018, ApJ, 865, 106
da Cunha E. et al., 2015, ApJ, 806, 110
da Cunha E., Charlot S., Elbaz D., 2008, MNRAS, 388, 1595
Danielson A. L. R. et al., 2017, ApJ, 840, 78
Demarco R. et al., 2010, ApJ, 711, 1185
Downes A. J. B., Peacock J. A., Savage A., Carrie D. R., 1986, MNRAS, 218, 31
Dunlop J. S., Peacock J. A., Savage A., Lilly S. J., Heasley J. N., Simon A. J. B., 1989, MNRAS, 238, 1171
Eisenhardt P. R. M. et al., 2008, ApJ, 684, 905
Elbaz D. et al., 2007, A&A, 468, 33
Elbaz D. et al., 2011, A&A, 533, A119
Engel H. et al., 2010, ApJ, 724, 233

Geach J. E. et al., 2006, ApJ, 649, 661
Geach J. E. et al., 2013, MNRAS, 432, 53
Geach J. E. et al., 2017, MNRAS, 465, 1789
González Delgado R. M. et al., 2017, A&A, 607, A128
Gunn J. E., Gott J. R. III, 1972, ApJ, 176, 1
Hainline L. J., Blain A. W., Smail I., Alexander D. M., Armus L., Chapman S. C., Ivison R. J., 2011, ApJ, 740, 96
Hancock P. J., Murphy T., Gaensler B. M., Hopkins A., Curran J. R., 2012, MNRAS, 422, 1812
Hancock P. J., Trott C. M., Hurley-Walker N., 2018, PASA, 35, e011
Hatch N. A., Muldrew S. I., Cooke E. A., Hartley W. G., Almaini O., Simpson C. J., Conselice C. J., 2016, MNRAS, 459, 387
Hatch N. A., Cooke E. A., Muldrew S. I., Hartley W. G., Almaini O., Conselice C. J., Simpson C. J., 2017, MNRAS, 464, 876
Hayashi M. et al., 2017, ApJ, 841, L21
Hayashi M. et al., 2018, ApJ, 856, 118
Hayashi M., Kodama T., Koyama Y., Tanaka I., Shimasaku K., Okamura S., 2010, MNRAS, 402, 1980
Hilton M. et al., 2010, ApJ, 718, 133
Hodge J. A. et al., 2013, ApJ, 768, 91
Holland W. S. et al., 2013, MNRAS, 430, 2513
Ilbert O. et al., 2015, A&A, 579, A2
Ivison R. J. et al., 2007, MNRAS, 380, 199
Jaffé Y. L. et al., 2018, MNRAS, 476, 4753
Johnston E. J., Aragón-Salamanca A., Merrifield M. R., 2014, MNRAS, 441, 333
Kauffmann G., White S. D. M., Heckman T. M., Ménard B., Brinchmann J., Charlot S., Tremonti C., Brinkmann J., 2004, MNRAS, 353, 713
Kettula K. et al., 2013, ApJ, 778, 74
Kocevski D. D. et al., 2011, ApJ, 736, 38
Kodama T., Balogh M. L., Smail I., Bower R. G., Nakata F., 2004, MNRAS, 354, 1103
Koyama Y., Kodama T., Shimasaku K., Hayashi M., Okamura S., Tanaka I., Tokoku C., 2010, MNRAS, 403, 1611
Koyama Y., Kodama T., Nakata F., Shimasaku K., Okamura S., 2011, ApJ, 734, 66
Lee-Brown D. B. et al., 2017, ApJ, 844, 43
Lotz J. M. et al., 2013, ApJ, 773, 154
Madau P., Dickinson M., 2014, ARA&A, 52, 415
Maughan B. J., Jones L. R., Ebeling H., Perlman E., Rosati P., Frye C., Mullis C. R., 2003, ApJ, 587, 589
Ma C. J. et al., 2015, ApJ, 806, 257
Mihos J. C., Hernquist L., 1994, ApJ, 425, L13
Muldrew S. I., Hatch N. A., Cooke E. A., 2015, MNRAS, 452, 2528
Muldrew S. I., Hatch N. A., Cooke E. A., 2018, MNRAS, 473, 2335
Mullis C. R., Rosati P., Lamer G., Böhringer H., Schwope A., Schuecker P., Fassbender R., 2005, ApJ, 623, L85
Muzzin A. et al., 2009, ApJ, 698, 1934
Navarro J. F., Frenk C. S., White S. D. M., 1996, ApJ, 462, 563
Nelan J. E., Smith R. J., Hudson M. J., Wegner G. A., Lucey J. R., Moore S. A. W., Quinney S. J., Suntzeff N. B., 2005, ApJ, 632, 137
Newman A. B., Ellis R. S., Andreon S., Treu T., Raichoor A., Trinchieri G., 2014, ApJ, 788, 51
Noble A. G., Webb T. M. A., Yee H. K. C., Muzzin A., Wilson G., van der Burg R. F. J., Balogh M. L., Shupe D. L., 2016, ApJ, 816, 48
Papovich C. et al., 2010, ApJ, 716, 1503
Pedregosa F. et al., 2011, J. Mach. Learn. Res., 12, 2825
Peng Y.-j. et al., 2010, ApJ, 721, 193
Popesso P. et al., 2012, A&A, 537, A58
Quadri R. F., Williams R. J., Franx M., Hildebrandt H., 2012, ApJ, 744, 88
Rettura A. et al., 2011, ApJ, 732, 94
Rosati P., Della Ceca R., Norman C., Giacconi R., 1998, ApJ, 492, L21
Rosati P. et al., 2004, AJ, 127, 230
Shimakawa R., Kodama T., Tadaki K.-I., Tanaka I., Hayashi M., Koyama Y., 2014, MNRAS, 441, L1
Simpson J. M. et al., 2014, ApJ, 788, 125
Smail I. et al., 2014, ApJ, 782, 19
Smith R. J., Lucey J. R., Hudson M. J., Allanson S. P., Bridges T. J., Hornschemeier A. E., Marzke R. O., Miller N. A., 2009, MNRAS, 392, 1265
Springel V. et al., 2005, Nature, 435, 629
Stach S. M. et al., 2018, ApJ, 860, 161
Stach S. M. et al., 2019, preprint (arXiv:1903.02602)
Stach S. M., Swinbank A. M., Smail I., Hilton M., Simpson J. M., Cooke E. A., 2017, ApJ, 849, 154
Stanford S. A. et al., 2006, ApJ, 646, L13
Stanford S. A., Holden B., Rosati P., Tozzi P., Borgani S., Eisenhardt P. R., Spinrad H., 2001, ApJ, 552, 504
Stanford S. A., Holden B., Rosati P., Eisenhardt P. R., Stern D., Squires G., Spinrad H., 2002, AJ, 123, 619
Strazzullo V. et al., 2013, ApJ, 772, 118
Swinbank A. M. et al., 2014, MNRAS, 438, 1267
Swinbank A. M., Chapman S. C., Smail I., Lindner C., Borys C., Blain A. W., Ivison R. J., Lewis G. F., 2006, MNRAS, 371, 465
Tadaki K.-i. et al., 2012, MNRAS, 423, 2617
Tanaka M., Kodama T., Arimoto N., Tanaka I., 2006, MNRAS, 365, 1392
Tanaka M., Finoguenov A., Ueda Y., 2010, ApJ, 716, L152
Thomas D., Maraston C., Bender R., Mendes de Oliveira C., 2005, ApJ, 621, 673
Tozzi P. et al., 2015, ApJ, 799, 93
Tran K.-V. H. et al., 2010, ApJ, 719, L126
Umetsu K., Tanaka M., Kodama T., Tanaka I., Futamase T., Kashikawa N., Hoshi T., 2005, PASJ, 57, 877
von der Linden A., Wild V., Kauffmann G., White S. D. M., Weinmann S., 2010, MNRAS, 404, 1231
Webb T. M. A., Yee H. K. C., Ivison R. J., Hoekstra H., Gladders M. D., Barrientos L. F., Hsieh B. C., 2005, ApJ, 631, 187
Webb T. M. A. et al., 2013, AJ, 146, 84
Weiß A. et al., 2009, ApJ, 707, 1201
Wilkinson A. et al., 2017, MNRAS, 464, 1380
Zeimann G. R. et al., 2013, ApJ, 779, 137
Ziparo F. et al., 2014, MNRAS, 437, 458

This paper has been typeset from a TEX/LATEX file prepared by the author.